Earth and Planetary Science Letters 512 (2019) 39–45

Contents lists available at ScienceDirect

Earth and Planetary Science Letters

www.elsevier.com/locate/epsl

Axial Seamount: Periodic tidal loading reveals stress dependence of the earthquake size distribution (*b* value)

Yen Joe Tan [a,*], Felix Waldhauser [a], Maya Tolstoy [a], William S.D. Wilcock [b]

[a] Lamont–Doherty Earth Observatory, Columbia University, Palisades, NY 10964, USA
[b] School of Oceanography, University of Washington, Seattle, WA 98195, USA

ARTICLE INFO

Article history:
Received 25 September 2018
Received in revised form 19 January 2019
Accepted 25 January 2019
Available online xxxx
Editor: M. Ishii

Keywords:
frequency–magnitude distribution
b value
earthquakes
tides

ABSTRACT

Earthquake size–frequency distributions commonly follow a power law, with the *b* value often used to quantify the relative proportion of small and large events. Laboratory experiments have found that the *b* value of microfractures decreases with increasing stress. Studies have inferred that this relationship also holds for earthquakes based on observations of earthquake *b* values varying systematically with faulting style, depth, and for subduction zone earthquakes, plate age. However, these studies are limited by small sample sizes despite aggregating events over large regions, which precludes the ability to control for other variables that might also affect earthquake *b* values such as rock heterogeneity and fault roughness. Our natural experiment in a unique seafloor laboratory on Axial Seamount involves analyzing the size–frequency distribution of ~60,000 microearthquakes which delineate a ring-fault system in a 25 km^3 block of crust that experiences periodic tidal loading of ±20 kPa. We find that above a threshold stress amplitude, *b* value is inversely correlated with tidal stress. The earthquake *b* value varies by ~0.09 per kPa change in Coulomb stress. Our results support the potential use of *b* values to estimate small stress variations in the Earth's crust.

1. Introduction

Earthquake occurrence is primarily controlled by the stress state on fault interfaces. Because *in situ* stress measurements are difficult to obtain, a proxy for estimating the stress state of fault zones through their seismic cycles is valuable for understanding earthquake occurrence and forecasting earthquakes. Earthquakes follow a power-law size–frequency distribution given as $\log_{10}(N) = a - bM$, where N is the number of earthquakes greater than or equal to magnitude M, and a and b are constants (Gutenberg and Richter, 1944). The value a describes the total number of earthquakes while the b value describes the relative frequency of small and large magnitude earthquakes. In rock fracture experiments, acoustic emissions from small cracking events follow the same power-law size distribution (Scholz, 1968). Furthermore, their b values have been found to decrease (larger proportion of large events) with increasing differential stress (Scholz, 1968; Amitrano, 2003; Goebel et al., 2013).

The same stress dependence of b value has been inferred to apply to earthquakes. The b value of earthquakes has been found to vary systematically with faulting style (Schorlemmer et al., 2005), depth (Spada et al., 2013), and for subduction zone earthquakes, plate age (Nishikawa and Ide, 2014). These observations are consistent with the earthquake b value decreasing with increasing differential stress (Scholz, 2015). However, these studies were restricted to using minimum bins of as few as 50 to 200 earthquakes to calculate the b values, which is barely a large enough sample size to even establish the existence of a power-law distribution (Stumpf and Porter, 2012). In addition, these studies had to aggregate events over large regions and thus were unable to control for other variables that might also affect earthquake b values such as rock heterogeneity (Mori and Abercrombie, 1997) and fault roughness (Goebel et al., 2017). Establishing whether earthquake b value varies systematically with stress is critical for demonstrating its potential use as a stress meter in the Earth's crust which could help improve forecasting of large earthquakes (Schorlemmer and Wiemer, 2005; Nanjo et al., 2012; Gulia et al., 2016) and volcanic eruptions (Kato et al., 2015).

Tidal forcing on the Earth produces periodic stress changes on the order of several kPa. Studies to establish a correlation between global earthquake rate and tidal stress changes have produced equivocal results (e.g. Emter, 1997, and references therein) with mainly negative results in continental regions (Vidale et al., 1998; Wang and Shearer, 2015). However, Cochran et al. (2004) found statistically-significant tidal triggering for shallow, subduction-zone

* Corresponding author.
E-mail address: yjt@ldeo.columbia.edu (Y.J. Tan).

https://doi.org/10.1016/j.epsl.2019.01.047
0012-821X/

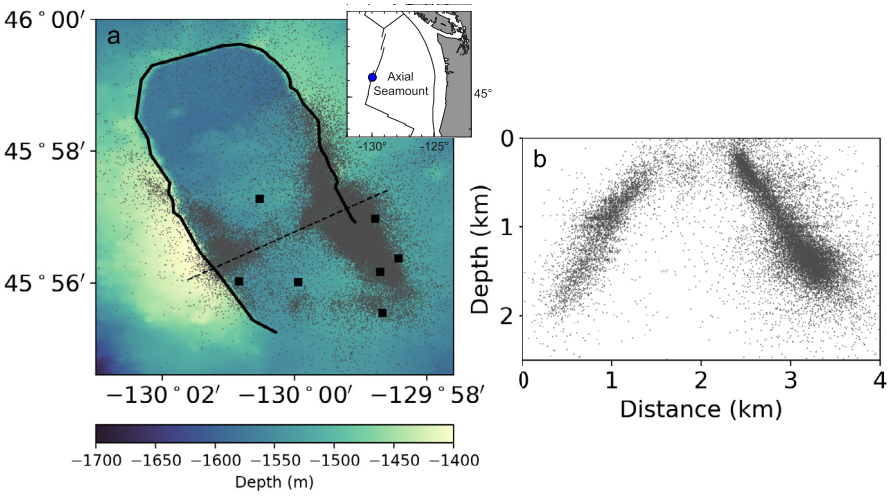

Fig. 1. Locations of ∼35,000 earthquakes above $M_c = 0.1$ between January 22nd and April 23rd 2015. (**a**) Bathymetric map with earthquake epicenters (grey dots), seismometers (black filled squares), caldera rim (black line), and the cross section shown in (b) (black dashed line). Inset shows regional location of Axial Seamount. (**b**) Depth cross-section across the caldera showing the projected earthquake locations within 0.5 km of the profile. (For interpretation of the colors in the figure(s), the reader is referred to the web version of this article.)

thrust earthquakes where stress changes due to ocean tidal loading can be an order of magnitude larger than the solid earth tides. Even stronger tidal triggering of earthquakes (Wilcock, 2001; Tolstoy et al., 2002; Stroup et al., 2007) that weakens post-eruption (Wilcock et al., 2016; Tan et al., 2018) has been documented at mid-ocean ridges. For instance, at Axial Seamount which is located at the intersection of the Juan de Fuca Ridge and the Cobb–Eickelberg hotspot, earthquakes occur preferentially during low ocean height (Tolstoy et al., 2002; Wilcock et al., 2016). Scholz et al. (2018) recently demonstrated that the exponential increase in seismicity rate with tidal stress at Axial Seamount agrees with predictions of both rate-state and stress corrosion theories (Scholz et al., 2018, Fig. 5), and the long-documented high sensitivity can be explained by the shallow depths of the earthquakes.

As part of the Ocean Observatory Initiative (OOI), a cabled seismic network was installed on the summit of Axial Seamount (Fig. 1a) with time-corrected seismic data streaming from late January 2015 (Wilcock et al., 2016). In the three months before the volcano erupted in April 2015, ∼60,000 earthquakes were located using the double-difference method (Waldhauser and Ellsworth, 2000). The earthquakes delineate an outward-dipping ring-fault system that extends to ∼2-km depth (Wilcock et al., 2016) (Fig. 1). The large number of events located within a small region, combined with the earthquakes' sensitivity to tidal stress perturbations (Wilcock et al., 2016; Scholz et al., 2018), make this an excellent natural laboratory to study how the earthquake b value relates to stress changes.

2. Methods

2.1. Earthquake catalog

In the first year of operation, ∼70,000 earthquakes were located by the OOI Axial seismic network (Wilcock et al., 2016). In the three months before the volcano erupted, the majority of the composite focal mechanisms determined showed normal or oblique-normal sense of motion. During the one-month-long eruption period, the slip direction was reversed as the volcano deflated (Levy et al., 2018). After the eruption, the seismicity rate decreased substantially (Wilcock et al., 2016, 2018) with the focal mechanisms suggesting heterogeneous fault slip directions (Levy et al., 2018). Therefore, in this paper, we only examine the ∼60,000 earthquakes that occurred in the three months before the volcano erupted. The earthquake catalog, including the moment magnitudes (M_W) estimated following Tréhu and Solomon (1983), has been previously published (Wilcock et al., 2016).

2.2. b value

We estimate the b values using the maximum likelihood method (Aki, 1965), accounting for the use of binned magnitudes (Utsu, 1966):

$$b = \frac{\log_{10} e}{\bar{M} - \left(M_c - \frac{\Delta M}{2}\right)}, \tag{1}$$

where M_c is the magnitude of completeness of the data set, $\bar{M}$ is the mean magnitude of earthquakes with magnitude $\geq M_c$, and ΔM is the binning interval of the magnitude, which is 0.1 in this study. We estimate the standard deviation of the b value estimate following Shi and Bolt (1982):

$$\delta b = 2.3 b^2 \sqrt{\frac{\sum_i^n (M_i - \bar{M})^2}{n(n-1)}}, \tag{2}$$

where n is the sample size. We quantify the significance of the b value difference between two groups of earthquakes using Utsu's test (Utsu, 1992):

$$p \approx \exp\left(\frac{-\Delta AIC}{2} - 2\right), \tag{3}$$

$$\Delta AIC = -2(N_1 + N_2)\ln(N_1 + N_2) + 2N_1 \ln\left(N_1 + \frac{N_2 b_1}{b_2}\right) + 2N_2 \ln\left(N_2 + \frac{N_1 b_2}{b_1}\right) - 2, \tag{4}$$

where p is the probability that the two groups of earthquakes are drawn from the same population, AIC is the Akaike's information criterion, N_1 and N_2 are the number of earthquakes, and b_1 and b_2 are the estimated b values of the two groups of earthquakes. We also compare the b value difference between two groups with their standard deviations (Kagan, 1997):

$$z = \frac{b_1 - b_2}{\sqrt{\sigma_1^2 + \sigma_2^2}}. \quad (5)$$

The null hypothesis that two b values come from the same population can be rejected at the 95% confidence level if z exceeds 1.96 and at the 99% confidence level if z exceeds 2.58.

2.3. Magnitude of completeness

We first estimate the magnitude of completeness (M_c) of the catalog using the point of maximum curvature of the frequency–magnitude distribution (FMD) (Wiemer and Katsumata, 1999), which is equivalent to finding the magnitude bin with the highest number of earthquakes in the non-cumulative FMD (Mignan and Woessner, 2012). We find $M_c = 0.0$ (Fig. S1). We then estimate M_c using the goodness-of-fit (GFT) method by comparing observed and synthetic cumulative FMDs (Wiemer and Wyss, 2000). We calculate synthetic cumulative FMDs using estimated a and b values of the observed earthquake catalog assuming a range of increasing cutoff magnitudes M_{co}. The goodness-of-fit is quantified using the parameter R:

$$R_{M_{co}} = 100 - \left(100 \frac{\sum_{M_{co}}^{M_{max}} |O_i - S_i|}{\sum_{M_{co}}^{M_{max}} O_i}\right), \quad (6)$$

where O_i and S_i are the observed and predicted number of earthquakes in each magnitude bin. M_c is then the first M_{co} where R exceeds a fixed threshold, typically defined at 90% level of fit (Wiemer and Wyss, 2000) because real catalogs rarely achieve 95% level of fit (Woessner and Wiemer, 2005). We obtain $M_c = -0.1$ when using a 90% fit threshold and $M_c = 0.1$ when using a 95% fit threshold (Fig. S1). Finally, we estimate M_c base on the b value stability as a function of assumed cutoff magnitude M_{co} (Cao and Gao, 2002). M_c is the first M_{co} at which $|b_{ave} - b| \leq \delta b$ (Woessner and Wiemer, 2005), with b_{ave} being the mean of the b values estimated for three successive M_{co} (magnitude range of 0.3 since the bin interval is 0.1) and δb being the standard deviation of the b value estimate (Shi and Bolt, 1982). We obtain $M_c = 0.3$ (Fig. S1).

The maximum curvature (MAXC) and the GFT-90% methods can underestimate M_c (Woessner and Wiemer, 2005) while the method based on b value stability (MBS) may overestimate M_c (Mignan and Woessner, 2012). Therefore, in this study, we adopt $M_c = 0.1$ from the GFT-95% method which leaves us with ~35,000 earthquakes above M_c and an estimated b value of 1.31 ± 0.01. We also consider the more conservative estimate of $M_c = 0.3$ from the MBS method, which leaves us with ~20,000 earthquakes above M_c and an estimated b value of 1.39 ± 0.01. The estimated b values are consistent with previous observations of $b > 1$ for normal fault events (Schorlemmer et al., 2005) and in marine volcanic environments (Bohnenstiehl et al., 2008).

2.4. Tidal stress

We estimate the horizontal strains due to body tides using the SPOTL software which assumes an elastic and spherical Earth (degree-two Love numbers $h = 0.6114$, $k = 0.3040$, and $l = 0.0832$) and computes the tidal strains directly from the positions of the Moon and the Sun (Agnew, 1997). We then calculate the vertical strain from the horizontal strains assuming a plane stress condition:

$$\Delta\epsilon_{zz} = \frac{-\nu}{1-\nu}(\Delta\epsilon_{xx} + \Delta\epsilon_{yy}), \quad (7)$$

using Poisson's ratio ν of 0.23 which is consistent with $V_P = 5.4$ km/s, $V_S = 3.2$ km/s, and a density of 2800 kg/m^3. The Poisson's ratio quantifies the effect where a material tends to contract along the axes perpendicular to the axis of tensile strain. For the effects of ocean tidal loading, we first obtain the predicted tidal height for the eight major short-period tidal constituents (K1, K2, M2, N2, O1, P1, Q1, and S2) using the EOT11a global ocean tidal model (Savcenko and Bosch, 2012) combined with the Oregon State University regional ocean tidal model for the west coast of the United States (Egbert and Erofeeva, 2002) as provided with the SPOTL software. We then calculate the ocean tidal loading effect in two parts. First, we estimate the horizontal strains due to variable regional ocean tidal loading using the SPOTL software, which uses a mass-loading Green's function for strain based on the Gutenberg-Bullen Earth model (Agnew, 1997). We then calculate the vertical strain from the horizontal strains assuming a plane stress condition before converting strains to stresses using elastic constants consistent with a Poisson's ratio of 0.23. Secondly, we estimate the vertical stress perturbation due to direct ocean tidal loading as

$$\Delta\sigma_{zz} = \rho g h, \quad (8)$$

where ρ is the density of seawater (1030 kg/m^3), g is the gravitational acceleration (9.8 m/s^2), and h is the tidal height relative to its mean value. We then estimate the horizontal stresses from the vertical stress assuming uniaxial strain:

$$\Delta\sigma_{xx} = \Delta\sigma_{yy} = \frac{\nu}{1-\nu}\Delta\sigma_{zz}. \quad (9)$$

Finally, we combine the various tidal stress components to form the stress tensor. We find that at Axial Seamount, ocean tides are much larger than body tides and hence the vertical tidal stress dominates (Fig. S2). We calculate the tidal-stress time series in 5-minute intervals. We assume the stresses estimated at the seafloor applies to the earthquake source region because the tidal wavelengths are very long compared to the earthquake depths of mostly less than 2 km (Fig. 1b). We do not account for the effect of bathymetry in our tidal stress calculations. The bathymetry only varies by less than 200 m around our earthquake epicenter region (Fig. 1a) and while it might affect the absolute value of our tidal stress estimates, the relative difference in tidal stress at different times is expected to still be valid.

We assume the earthquakes are predominantly normal faulting events since the ring-fault system appears to have accommodated pre-eruptive inflation (Wilcock et al., 2016), 79% (31 of 39) of the composite focal mechanisms determined before the eruption based on first-motion polarity showed normal or oblique-normal sense of motion (Levy et al., 2018), and this is a region of tectonic extension. This initially seems to contradict the well-documented preferential occurrence of earthquakes during low ocean height at Axial Seamount (Tolstoy et al., 2002; Wilcock et al., 2016) because a decrease in ocean height (increase in tensile vertical stress) should produce a Coulomb stress change that inhibits slip on normal faults. However, Scholz et al. (2018) resolved this apparent paradox by accounting for the effect of the underlying magma chamber on the stress distribution. The higher compressibility of the magma chamber means that it will inflate or deflate relative to the surrounding crust in response to tidal stresses and produce Coulomb stress changes on the fault that is opposite in sign as those produced directly by the tidal stresses (Scholz et al., 2018, Fig. 3). When the magma chamber bulk modulus is below a critical value, the magma chamber effect will exceed that of the direct tidal stress effect and the phase of the tidal triggering gets inverted (Scholz et al., 2018, Fig. 4), as observed at Axial Seamount. Since the vertical tidal stress dominates at Axial Seamount (Fig. S2) and the average Coulomb stress change on the fault can be approximated as $\Delta CFS = \chi\sigma_{zz}$ with χ dependent on the magma chamber bulk modulus (Scholz et al., 2018), we will focus on variations in

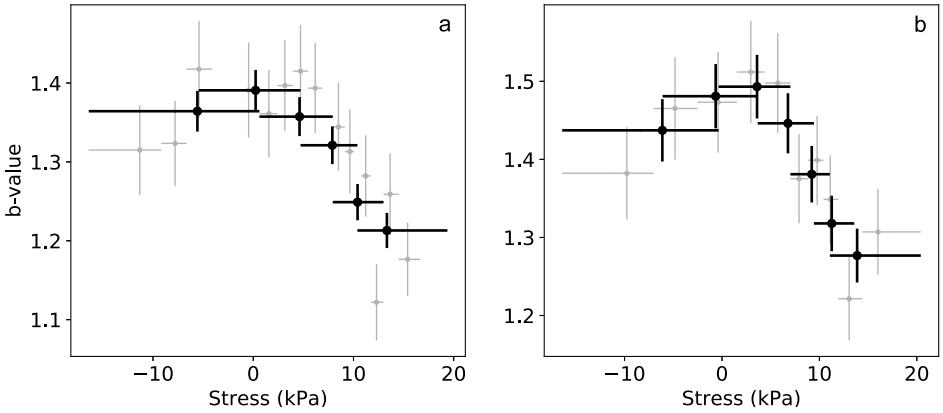

Fig. 2. The earthquake b value as a function of tidal stress. The vertical error bars represent two standard deviations of the estimated b values (Shi and Bolt, 1982). The horizontal bars represent the range of earthquake tidal stress values included in each bin, with the markers centered at the mean earthquake tidal stress for each bin. (**a**) Using $M_c = 0.1$. Non-overlapping bins of 2,000 events (gray) as well as moving bins of 10,000 events shifted by 5,000 events (black). (**b**) Using $M_c = 0.3$. Non-overlapping bins of 2,000 events (gray) as well as moving bins of 5,000 events shifted by 2,500 events (black).

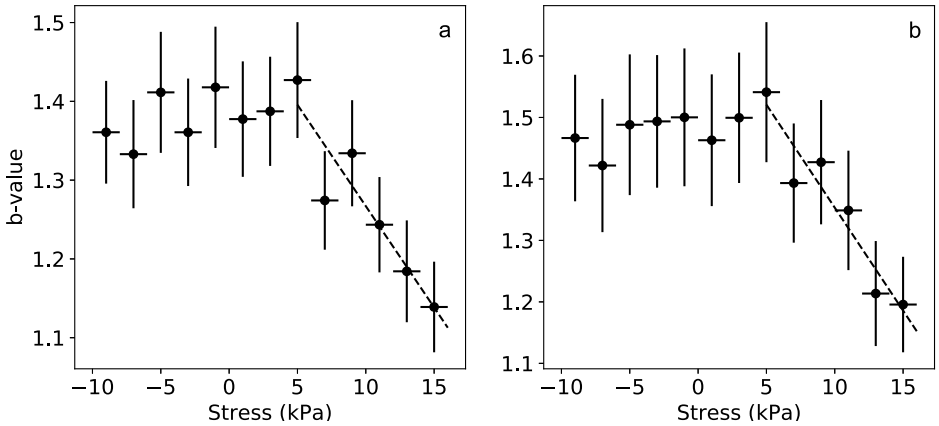

Fig. 3. The earthquake b values for non-overlapping stress bins of 2 kPa. The vertical error bars represent two standard deviations of the estimated b values from bootstrapping. The horizontal bars represent the tidal stress range for each bin. Dashed lines represent linear least-squares fits, both giving b value varying by ∼0.03 per kPa. (**a**) Using $M_c = 0.1$. (**b**) Using $M_c = 0.3$.

vertical stress due to the combined effects of ocean tidal loading and body tide. We adopt tension as positive and an increase in vertical stress represents an increase in encouraging stress (Coulomb stress change that favors slip on normal fault). The vertical tidal stress has estimated amplitudes of ±20 kPa (Fig. S2).

3. Results

We assign each earthquake a tidal stress value based on its origin time. After sorting the earthquakes based on their associated tidal stress values, we calculate the b values for non-overlapping bins of 2,000 events. When using $M_c = 0.1$, we also calculate the b values for moving bins of 10,000 events, shifted by 5,000 events. When using $M_c = 0.3$, we calculate the b values for moving bins of 5,000 events, shifted by 2,500 events. For each bin, we re-estimate M_c using the GFT-95% method and only keep the data point if the re-estimated M_c equals the M_c of the bulk data. Only 3 out of 40 data points did not fulfill the criteria. We find that the earthquake b value only decreases systematically with increasing tidal stress when stress amplitudes exceed a certain threshold (Fig. 2).

We further investigate the relationship between b value and tidal stress by looking at how the b value varies between fixed stress bins. We calculate the b values for non-overlapping bins of 2 kPa for stress values between −10 and 16 kPa. We pick this range because it incorporates ∼92% of the earthquakes (Fig. S3) and allows us to use a reasonably large number of events per stress bin. The number of events vary between stress bins (Fig. S3) so we adopt the following strategy to maintain consistency: For each stress bin, we estimate 1,000 b values using events randomly drawn with replacement from the earthquake population. When using $M_c = 0.1$, we draw 1,300 events for each b value calculation because the stress bin with the smallest number of events contains ∼1,300 earthquakes (Fig. S3). When using $M_c = 0.3$, we draw 700 events for each b value calculation. The reported b value is then the average b value from the bootstrapping. We find that at low stress values, the b values are high but remain relatively constant. However, at stress amplitudes greater than 5 kPa, the earthquake b value decreases linearly with increasing tidal stress at ∼0.03 per kPa (Fig. 3).

We test the statistical significance of the b value variations as follows: Using $M_c = 0.3$, we sort the earthquakes based on their associated tidal stress values before splitting them into two equal-size groups. The lower tidal stress group has a mean stress of −1 kPa while the higher tidal stress group has a mean stress of 11 kPa. We further verified that the lower and higher tidal stress groups both have $M_c = 0.3$. We then plot the cumulative and non-cumulative FMDs. The cumulative FMD curves show increasing separation at larger magnitudes. The non-cumulative FMD curves intersect at around $M_w = 0.5$ (Fig. 4). These results show that the slopes of the FMD curves for the lower tidal stress group is steeper (larger b value) than that of the higher tidal stress group. The lower tidal stress group has a b value of 1.46 ± 0.01 while the

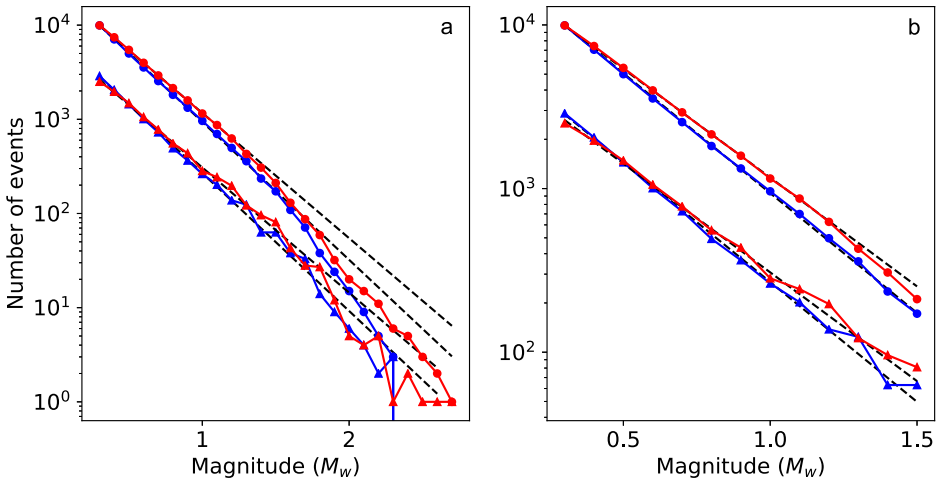

Fig. 4. Cumulative (circle) and non-cumulative (triangle) FMDs of two groups of earthquakes. Dashed lines indicate maximum-likelihood fits to the data. (**a**) Using $M_c = 0.3$, the ~20,000 earthquakes are split into two equal-size groups after being sorted based on their tidal stress values. The lower tidal stress group (blue) has a mean stress of −1 kPa while the higher tidal stress group (red) has a mean stress of 11 kPa. (**b**) Zoom-in of (**a**).

higher tidal stress group has a b value of 1.33 ± 0.01. We obtain similar b values and standard deviations from bootstrapping. The b value difference between the two groups are statistically significant at a <1% level based on both the Utsu's test (Utsu, 1992) and the z-test (see Methods).

The FMD curves deviate from linearity at large magnitudes. This could reflect a real departure from the power law distribution at large magnitudes or simply statistical fluctuations due to undersampling. To quantify how this affects our results, we repeat the b value calculations after excluding earthquakes of M_w greater than 1.5 where the FMD curves become nonlinear (Kagan, 1997) (Fig. 4). The lower tidal stress group now has an estimated b value of 1.53 ± 0.01 while the higher tidal stress group has an estimated b value of 1.40 ± 0.01. The b value difference between the two groups remains statistically significant at a <1% level based on both the Utsu's test (Utsu, 1992) and the z-test. We also repeat the analysis shown in Fig. 3 and while the absolute b values become larger, we obtain similar trends with the earthquake b value decreasing linearly with increasing tidal stress at ~0.03 per kPa when stress amplitude exceeds 5 kPa (Fig. S4). This is unsurprising because the maximum-likelihood estimate of the b value uses the average earthquake magnitude (Eq. (1)) and is therefore only slightly affected by the small number of large magnitude events.

We further verified that the minimum bin sizes often used to document b value variations (Schorlemmer et al., 2005; Spada et al., 2013; Nishikawa and Ide, 2014) are insufficient to robustly constrain our observed effect. We determine the minimum bin size needed to resolve the b value variations we observe as follows: Using $M_c = 0.3$, we sort the earthquakes based on their associated tidal stress values and split them into two equal-size groups (see Fig. 4). For a range of bin sizes, we then calculate 1,000 b values using events randomly drawn without replacement from the original population. The reported b value is then the average b value from the bootstrapping with the associated uncertainties (Fig. 5). For the b value difference between the lower and higher tidal stress groups to be statistically significant at a <5% and <1% level based on the Utsu's test (Utsu, 1992), we need minimum bin sizes of 900 and 1,600 respectively. For the b value difference between the two groups to be statistically significant at a <5% and <1% level based on the z-test, we need minimum bin sizes of 800 and 1,300 respectively.

In multiple continental regions, earthquake b values have been found to decrease with increasing depth which has been interpreted as the result of increasing crustal strength (Spada et al., 2013) and material homogeneity (Mori and Abercrombie, 1997) with depth. We similarly find that at Axial Seamount, the earthquake b value decreases with increasing depth (Fig. S5). Therefore, our observation of b value decreasing with increasing tidal stress could simply reflect the average earthquake depth increasing with tidal stress. While the Chi-squared test suggests the earthquake depth distributions of the lower and higher tidal stress groups come from two different populations, the depth difference is such that the mean and median depths of the higher tidal stress group is shallower by ~18 m and ~16 m respectively. We also find that the mean and median earthquake depth decrease with increasing tidal stress (Fig. S6). Since b value decreases with increasing depth, this change in depth distribution would have resulted in b value increasing with tidal stress. Therefore, our observation of earthquake b value decreasing with increasing tidal stress is unlikely to be a secondary effect of change in earthquake depth distribution with tides.

The earthquake spatial distribution of the lower and higher tidal stress groups also differs slightly, with relatively more events on the western and northeastern walls of the caldera for the lower tidal stress group (Fig. S7). We verify that the b value variation with tidal stress that we observe is still valid at smaller spatial scale as follows: We first bin the earthquakes into 1 km^2 spatial grids and find that there are five bins with more than 1,000 events (Fig. S7c). For each of these five bins, we sort the earthquakes base on their tidal stress values and split the events into two equal-size groups. We find that for four out of the five bins, the b value of the lower tidal stress group is larger than the higher tidal stress group. However, the statistical significance of the b value differences is not guaranteed by the Utsu's (Utsu, 1992) and z-test due to the small number of events in each bin.

4. Discussions

Scholz (2015) calibrated the stress dependence of earthquake b values assuming a simple frictional strength model combined with measurements of b value variation with depth at different tectonic environments (Spada et al., 2013) and found that b value varies by ~0.001 MPa^{-1}. Our analysis suggests that earthquake b value at Axial Seamount varies by ~0.03 kPa^{-1} (Fig. 3). In a recent tidal triggering study at Axial Seamount, Scholz et al. (2018) modeled the average Coulomb stress change on the 67° outward-dipping normal faults (Levy et al., 2018) (Fig. 1) due to vertical tidal stress changes as $\Delta CFS = \chi \sigma_{zz}$, with $\chi = 0.32$ for a realistic magma

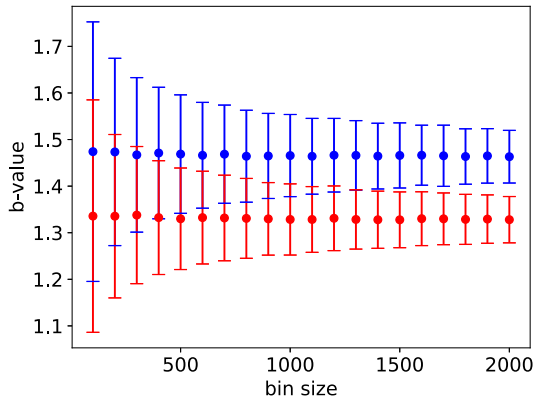

Fig. 5. The estimated earthquake b values for the lower (blue) and higher (red) tidal stress groups as a function of bin sizes. For each bin size, we calculate 1,000 b values using events randomly drawn without replacement from the original population. The reported b value is then the average b value from the bootstrapping. The vertical error bars represent two standard deviations.

chamber bulk modulus of 1 GPa. Adopting $\chi = 0.32$ would give us a b value change of $\sim$0.09 kPa^{-1} of Coulomb stress change. Our observation of b value variation that is sensitive to small stress perturbations ($\sim 10^5$ more sensitive compared to Scholz (2015)) is consistent with the long-documented observations of strong tidal triggering of earthquakes at Axial Seamount (Tolstoy et al., 2002; Wilcock et al., 2016) and other mid-ocean ridges (Wilcock, 2001; Stroup et al., 2007). Scholz et al. (2018) demonstrated that the seismicity rate change with tidal stress at Axial Seamount agrees with predictions of both rate-state and stress corrosion theories, and that the higher sensitivity can be explained by the shallow depths of the earthquakes (and hence the corresponding lower normal stress and stress drop values). The same explanation could apply to our observations since laboratory experiments previously showed that b value variations depend on stress normalized to the maximum failure strength (Scholz, 1968). Our observed greater sensitivity is also consistent with observation of the b value of acoustic emissions in the laboratory varying with tidal stress (Iwata and Young, 2005).

While our calibrated b value change with stress cannot be directly applied to other tectonic environments as most catalogued earthquakes occur at deeper depths, a sensitivity that is greater than 0.001 MPa^{-1} (Scholz, 2015) could explain observations of b value decreasing preceding large earthquakes (Nanjo et al., 2012) and volcanic eruption (Kato et al., 2015). Otherwise, these observations would represent stress changes on the order of 100 MPa in the decades before the Tohoku and Sumatra earthquakes (Nanjo et al., 2012) and weeks before the Mount Ontake eruption (Kato et al., 2015). Alternatively, these documented b value decreases might not have resulted from stress increases. Based on epidemic-type aftershock sequence (ETAS) modeling, Helmstetter et al. (2003) suggested that such b value decreases can emerge simply from conditioning of the seismicity having to culminate in a mainshock, which results in there being a growing contribution of a deviatoric power law distribution with a smaller b value to the background unconditional distribution. At Axial Seamount, Bohnenstiehl et al. (2018) did not observe a systematic decrease in b value leading up to the April 2015 eruption. Wilcock et al. (2016) similarly did not observe the tidal triggering signal or the seismicity rate increasing leading up to the eruption. Therefore, the presumed stress accumulation in the three months before the volcano erupted might be too small to be detected with the current dataset.

Our observed stress dependence of earthquake b values can be understood within the same statistical model first proposed to explain why the b values of microfractures in laboratory experiments vary with stress (Scholz, 1968). If we treat the Earth's crust as an inhomogeneous elastic medium experiencing a uniform applied stress, the presence of inhomogeneities means that the stress at each point within the crust is a random variable that follows a probability distribution function that depends on the uniform applied stress. If we further assume that at each point, fracture will occur if the local stress exceeds a critical value and that fractures stop growing when they propagate into a region of lower stress, it follows that a fracture has a higher probability of growing larger when the applied stress is greater (Scholz, 1968). This translates to a decrease in b value with increasing stress. However, the threshold effect that we observe is not well-explained by this model. Nevertheless, a similar threshold effect is often discussed for earthquake triggering from stress changes (Roy and Marone, 1996; Hardebeck et al., 2003) with the stress threshold being dependent on the fault stiffness (Roy and Marone, 1996).

A recent study using global data hinted at a b value-tidal stress correlation, as earthquake b values were found to decrease with increasing tidal shear stress ranking, where an earthquake's ranking is based on the maximum tidal shear stress during the day before the earthquake relative to the daily maxima in the 15 days before the earthquake (Ide et al., 2016). However, the relationship was not clear for earthquakes smaller than M_w 6.5 when looking at the Global Centroid Moment Tensor catalogue, potentially due to aggregating events of various faulting styles in diverse tectonic regimes (Ide et al., 2016). Due to the lack of a strong correlation between global seismicity rate and tidal stress changes (e.g. Emter, 1997, and references therein), the authors invoke enhanced slow slip during increased tidal stresses that subsequently triggers earthquakes and increases the probability of rupture growth (Ide et al., 2016). However, at Axial Seamount, the sensitivity of the earthquakes to small tidal stress changes (Tolstoy et al., 2002; Wilcock et al., 2016) can be simply explained by the shallow depths of the earthquakes (Scholz et al., 2018) without invoking the existence of slow slip.

5. Conclusions

Our natural experiment in a unique seafloor laboratory, looking at the size distribution of earthquakes in a 25 km^3 block of crust that experiences periodic tidal loading, provides a robust validation of the stress dependence of the earthquake b value. We find that above a certain threshold stress amplitude, the earthquake b value decreases linearly with increasing tidal stress. The b value varies by $\sim$0.09 per kPa change in Coulomb stress. This suggests that b value changes can be used to estimate stress variations in the Earth's crust.

Acknowledgements

Y. J. T. thanks Göran Ekstrom, David Marsan, Meredith Nettles, Christopher Scholz, and Spahr Webb for fruitful discussions. This work was supported by NSF under grant OCE-1536320. The earthquake catalog used in this study is from Wilcock et al. (2016) and is archived in the Interdisciplinary Earth Data Alliance Marine Geoscience Data System (https://doi.org/10.1594/IEDA/323843). The authors thank Suguru Yabe and two anonymous reviewers for their constructive comments that improved the manuscript.

Appendix A. Supplementary material

Supplementary material related to this article can be found online at https://doi.org/10.1016/j.epsl.2019.01.047.

References

Agnew, D., 1997. NLOADF: a program for computing ocean-tide loading. J. Geophys. Res. 102, 5109–5110.

Aki, K., 1965. Maximum likelihood estimate of b in the formula $\log N = a - bM$ and its confidence limits. Bull. Earthq. Res. Inst. 43, 237–239.

Amitrano, D., 2003. Brittle–ductile transition and associated seismicity: experimental and numerical studies and relationship with the b value. J. Geophys. Res. 108 (B1). https://doi.org/10.1029/2001JB000680.

Bohnenstiehl, D.R., Waldhauser, F., Tolstoy, M., 2008. Frequency–magnitude distribution of microearthquakes beneath the 9°50′N region of the East Pacific Rise, October 2003 through April 2004. Geochem. Geophys. Geosyst. 9 (10), Q10T03. https://doi.org/10.1029/2008GC002128.

Bohnenstiehl, D.R., et al., 2018. Spatial, temporal and size–frequency characteristics of microearthquake sequences leading up to the 2015 eruption of Axial Seamount. In: AGU Fall Meeting 2018. Eos V52B-02.

Cao, A.M., Gao, S.S., 2002. Temporal variations of seismic b-values beneath northeastern japan island arc. Geophys. Res. Lett. 29. https://doi.org/10.1029/2001GL013775.

Cochran, E.S., Vidale, J.E., Tanaka, S., 2004. Earth tides can trigger shallow thrust fault earthquakes. Science 306, 1164–1166. https://doi.org/10.1126/science.1103961.

Egbert, G.D., Erofeeva, S.Y., 2002. Efficient inverse modeling of barotropic ocean tides. J. Atmos. Ocean. Technol. 19, 183–204.

Emter, D., 1997. Tidal triggering of earthquakes and volcanic events. In: Bhattacharji, S., et al. (Eds.), Tidal Phenomena. Springer, New York, pp. 293–309.

Goebel, T.H.W., Schorlemmer, D., Becker, T.W., Dresen, G., Sammis, C.G., 2013. Acoustic emissions document stress changes over many seismic cycles in stick-slip experiments. Geophys. Res. Lett. 40, 2049–2054. https://doi.org/10.1002/grl.50507.

Goebel, T.H.W., Kwiatek, G., Becker, T.W., Brodsky, E.E., Dresen, G., 2017. What allows seismic events to grow big? Insights from b-value and fault roughness analysis in laboratory stick-slip experiments. Geology 45, 815–818.

Gulia, L., Tormann, T., Wiemer, S., Herrmann, M., Seif, S., 2016. Short-term probabilistic earthquake risk assessment considering time-dependent b values. Geophys. Res. Lett. 43, 1100–1108.

Gutenberg, B., Richter, C., 1944. Frequency of earthquake in California. Bull. Seismol. Soc. Am. 34, 185–188.

Hardebeck, J.L., Nazareth, J.J., Hauksson, E., 2003. The static stress change triggering model: constraints from two southern California aftershock sequences. J. Geophys. Res. 103, 24,427–24,437.

Helmstetter, A., Sornette, D., Grasso, J., 2003. Mainshocks are aftershocks of conditional foreshocks: how do foreshock statistical properties emerge from aftershock laws. J. Geophys. Res. 108. https://doi.org/10.1029/2002JB001991.

Ide, S., Yabe, S., Tanaka, Y., 2016. Earthquake potential revealed by tidal influence on earthquake size–frequency statistics. Nat. Geosci. 9, 834–837. https://doi.org/10.1038/NGEO2796.

Iwata, T., Young, R.P., 2005. Tidal stress/strain and the b-values of acoustic emissions at the Underground Research Laboratory, Canada. Pure Appl. Geophys. 162, 1291–1308. https://doi.org/10.1007/s00024-005-2670-2.

Kagan, Y.Y., 1997. Seismic moment–frequency relation for shallow earthquakes: regional comparison. J. Geophys. Res. 102, 2835–2852.

Kato, A., et al., 2015. Preparatory and precursory processes leading up to the 2014 phreatic eruption of Mount Ontake, Japan. Earth Planets Space 67. https://doi.org/10.1186/s40623-015-0288-x.

Levy, S., et al., 2018. Mechanics of fault reactivation before, during, and after the 2015 eruption of Axial Seamount. Geology. https://doi.org/10.1130/G39978.1.

Mignan, A., Woessner, J., 2012. Estimating the magnitude of completeness for earthquake catalogs. Commun. Online Resour. Stat. Seism. Anal. https://doi.org/10.5078/corssa-00180805.

Mori, J., Abercrombie, R.E., 1997. Depth dependence of earthquake frequency–magnitude distributions in California: implications for rupture initiation. J. Geophys. Res. 102, 15,081–15,090.

Nanjo, K.Z., Hirata, N., Obara, K., Kasahara, K., 2012. Decade-scale decrease in b value prior to the M9-class 2011 Tohoku and 2004 Sumatra quakes. Geophys. Res. Lett. 39, L20304.

Nishikawa, T., Ide, S., 2014. Earthquake size distribution in subduction zones linked to slab buoyancy. Nat. Geosci. 7, 904–908. https://doi.org/10.1038/NGEO2279.

Roy, M., Marone, C., 1996. Earthquake nucleation on model faults with rate- and state-dependent friction: effects of inertia. J. Geophys. Res. 101, 13,919–13,923.

Savcenko, R., Bosch, W., 2012. EOT11a – Empirical Ocean Tide Model from Multi-Mission Satellite Altimetry. DGFI Report No. 89.

Scholz, C.H., 1968. The frequency–magnitude relation of microfracturing in rock and its relation to earthquakes. Bull. Seismol. Soc. Am. 58, 399–415.

Scholz, C.H., 2015. On the stress dependence of the earthquake b value. Geophys. Res. Lett. 42, 1399–1402. https://doi.org/10.1002/2014GL062863.

Scholz, C.H., Tan, Y.J., Albino, F., 2018. The mechanism of tidal triggering of earthquakes at mid-ocean ridges. arXiv:1812.00639v1.

Schorlemmer, D., Wiemer, S., 2005. Microseismicity data forecast rupture area. Nature 434, 1,086.

Schorlemmer, D., Wiemer, S., Wyss, M., 2005. Variations in earthquake-size distribution across different stress regimes. Nature 437, 539–542.

Shi, Y., Bolt, B.A., 1982. The standard error of the magnitude–frequency b value. Bull. Seismol. Soc. Am. 72 (5), 1677–1687.

Spada, M., Tormann, T., Wiemer, S., Enescu, B., 2013. Generic dependence of the frequency–size distribution of earthquakes on depth and its relation to the strength profile of the crust. Geophys. Res. Lett. 40, 709–714. https://doi.org/10.1029/2012GL054198.

Stroup, D.F., Bohnenstiehl, D.R., Tolstoy, M., Waldhauser, F., Weekly, R.T., 2007. Pulse of the seafloor: tidal triggering of microearthquakes at 9°50′N East Pacific Rise. Geophys. Res. Lett. 34, L15301. https://doi.org/10.1029/2007GL030088.

Stumpf, M., Porter, M., 2012. Critical truths about power laws. Science 335, 665–666.

Tan, Y.J., Tolstoy, M., Waldhauser, F., Bohnenstiehl, D.R., 2018. Tidal triggering of microearthquakes over an eruption cycle at 9°50′N East Pacific Rise. Geophys. Res. Lett. 45, 1825–1831.

Tolstoy, M., Vernon, F.L., Orcutt, J.A., Wyatt, F.K., 2002. Breathing of the seafloor: tidal correlations of seismicity at Axial Volcano. Geology 30, 503–506.

Tréhu, A.M., Solomon, S.C., 1983. Earthquakes in the Orozco transform zone: seismicity, source mechanisms, and tectonics. J. Geophys. Res. 88 (B10), 8203–8225.

Utsu, T., 1966. A statistical significance test of the difference in b-value between two earthquake groups. J. Phys. Earth 14, 34–40.

Utsu, T., 1992. On seismicity. Rep. Jt. Res. Inst. Stat. Math. 34, 139–157.

Vidale, J., Agnew, D., Johnston, M., Oppenheimer, D., 1998. Absence of earthquake correlation with earth tides: an indication of high preseismic fault stress rate. J. Geophys. Res. 103 (24), 567–572.

Waldhauser, F., Ellsworth, W.L., 2000. A double-difference earthquake location and algorithm: method and application to the northern Hayward Fault, California. Bull. Seismol. Soc. Am. 90, 1353–1368. https://doi.org/10.1785/0120000006.

Wang, W., Shearer, P.M., 2015. No clear evidence for localized tidal periodicities in earthquakes in the central Japan region. J. Geophys. Res. 120, 6317–6328. https://doi.org/10.1002/2015jb011937.

Wiemer, S., Katsumata, K., 1999. Spatial variability of seismicity parameters in aftershock zones. J. Geophys. Res. 103, 13135–13151.

Wiemer, S., Wyss, M., 2000. Minimum magnitude of completeness in earthquake catalogs: examples from Alaska, the western United States, and Japan. Bull. Seismol. Soc. Am. 90, 859–869. https://doi.org/10.1785/0119990114.

Wilcock, W.S.D., 2001. Tidal triggering of microearthquakes on the Juan de Fuca Ridge. Geophys. Res. Lett. 28, 3999–4002.

Wilcock, W.S.D., et al., 2016. Seismic constraints on caldera dynamics from the 2015 Axial Seamount eruption. Science 354 (6318), 1395–1399.

Wilcock, W.S.D., et al., 2018. The recent volcanic history of Axial Seamount: geophysical insights into past eruption dynamics with an eye toward enhanced observations of future eruptions. Oceanography 31 (1), 114–123.

Woessner, J., Wiemer, S., 2005. Assessing the quality of earthquake catalogues: estimating the magnitude of completeness and its uncertainty. Bull. Seismol. Soc. Am. 95, 684–698. https://doi.org/10.1785/0120040007.

Supporting Information for

"Axial Seamount: Periodic tidal loading reveals stress dependence of the earthquake size distribution (*b* value)"

Yen Joe Tan[1,*], Felix Waldhauser[1], Maya Tolstoy[1], and William S.D. Wilcock[2]

[1]Lamont-Doherty Earth Observatory, Columbia University, Palisades, NY 10964, USA.

[2]School of Oceanography, University of Washington, Seattle, WA 98195, USA.

Corresponding author: Y.J. Tan, yjt@ldeo.columbia.edu

1. Figure S1

Selection of the minimum magnitude of completeness (M_c). **top**, Cumulative (triangle) and non-cumulative (circle) frequency-magnitude distributions (FMDs). Dashed lines depict the M_c estimates based on the MAXC (green), GFT-90% (blue), GFT-95% (red), and MBS (magenta) methods. **middle**, Variation of parameter R used to quantify the goodness-of-fit between observed and synthetic cumulative FMDs for a range of cutoff magnitudes. Dashed lines depict the 90% (blue) and 95% (red) thresholds. **bottom**, Variation of the b value for a range of cutoff magnitudes. Dashed line depicts where the b value first stabilizes (see Methods).

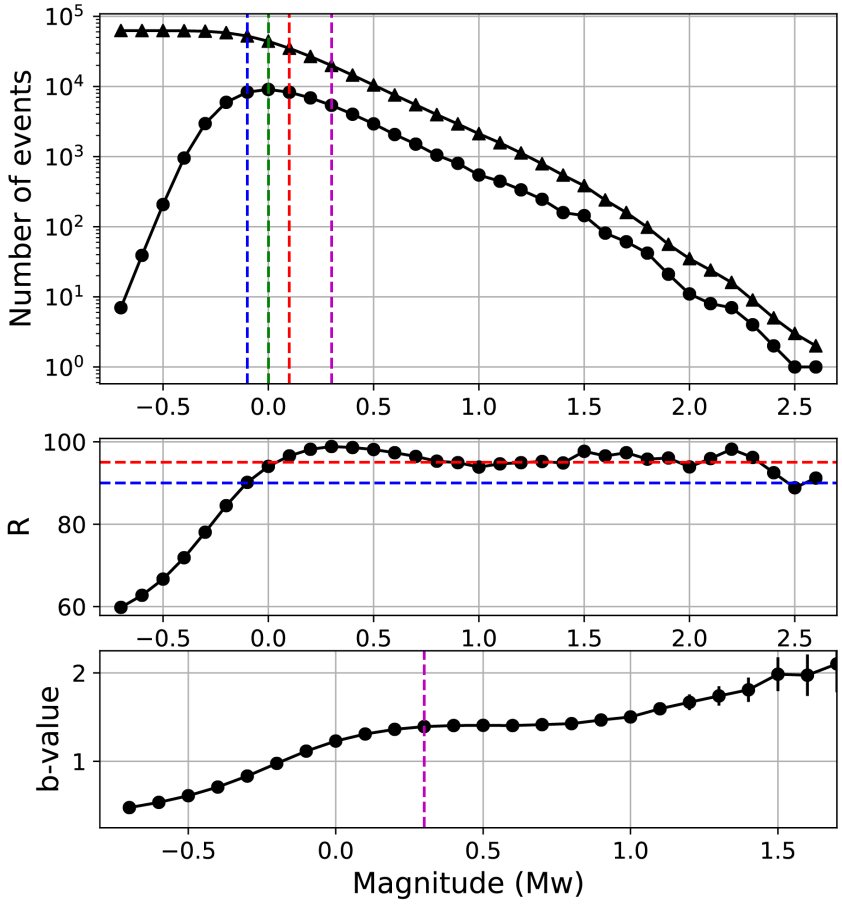

2. Figure S2

Time series of predicted tides at the surface at 45.95°N, 130.00°W. **top**, Estimate of σ_{xx} (black), σ_{yy} (blue), and σ_{zz} (red) from ocean tidal loading, with tension being positive (i.e. σ_{zz} is positive upwards). **bottom**, Body tides. The stress amplitude is about an order of magnitude smaller than that of ocean tides.

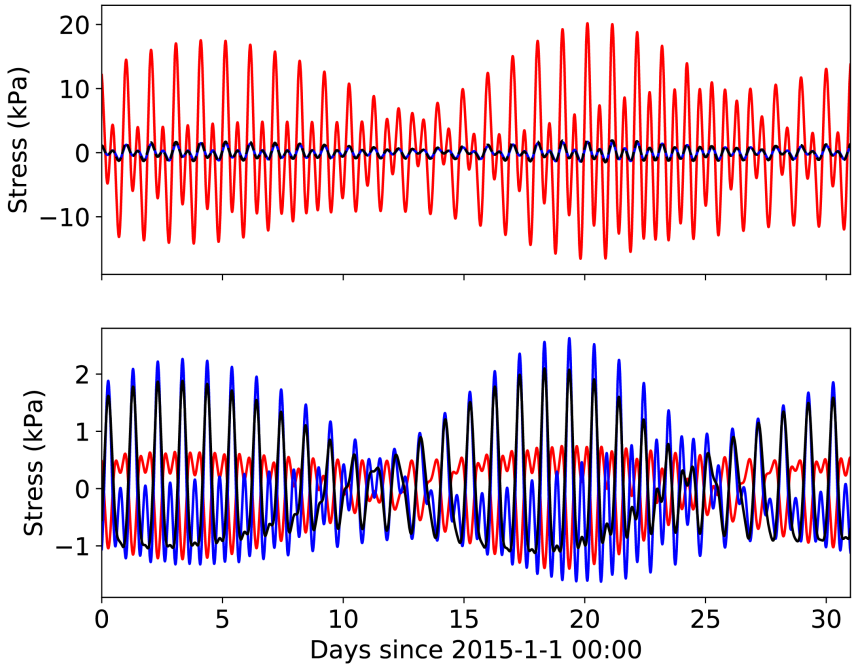

3. Figure S3

The earthquake tidal stress distribution in bins of 2 kPa for M_c = 0.1 (blue) and M_c = 0.3 (grey). The distribution reflects the combined effect of seismicity rate increasing with tidal stress [*Scholz et al.*, 2018] and the uneven distribution of tidal stress amplitudes.

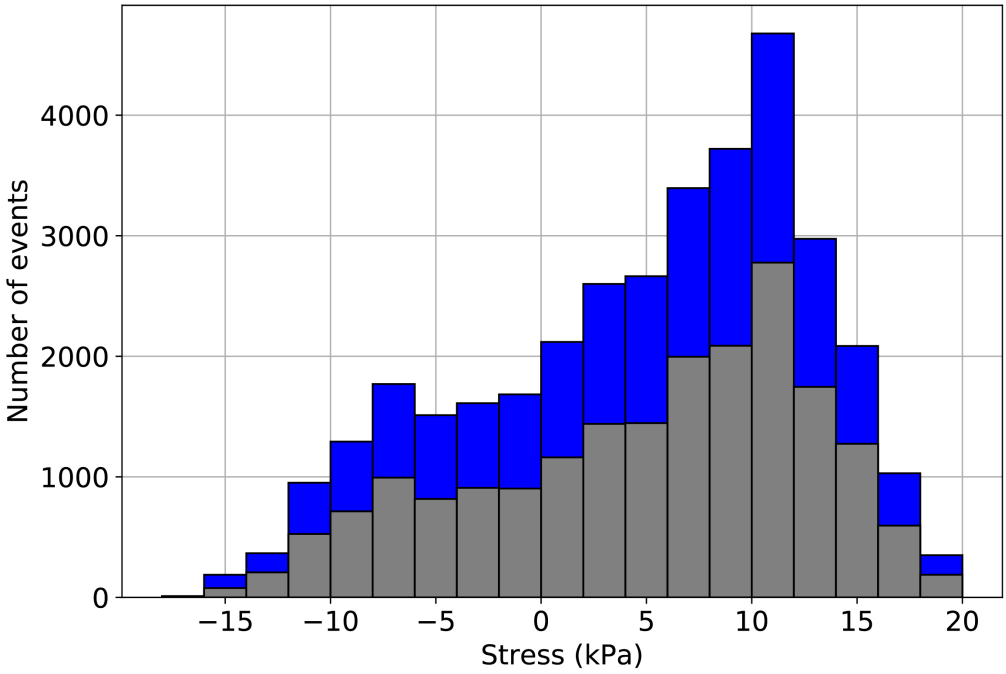

4. Figure S4

The earthquake b values for non-overlapping stress bins of 2 kPa. Earthquakes of M_w greater than 1.5 are excluded. The vertical error bars represent two standard deviations of the estimated b values from bootstrapping. The horizontal bars represent the tidal stress range for each bin. Dashed lines represent linear least-squares fits, both giving b value varying by ~ 0.03 per kPa. **a**, Using $M_c = 0.1$. **b**, Using $M_c = 0.3$.

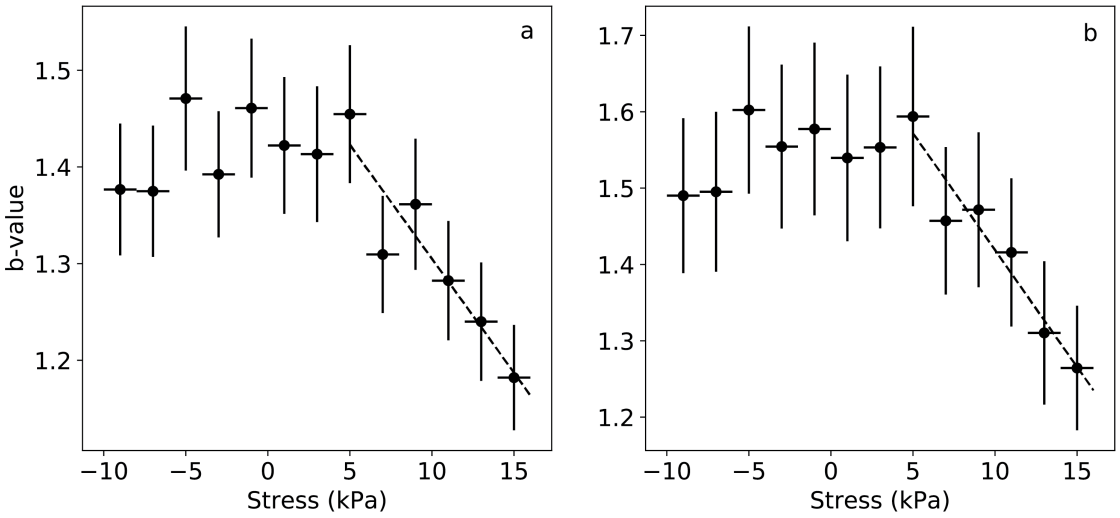

5. Figure S5

The earthquake b value as a function of depth in non-overlapping bins of 2,500 earthquakes. The vertical error bars represent two standard deviations [*Shi and Bolt*, 1982] of the estimated b values. The horizontal bars represent the range of earthquake depth values included in each bin. Since M_c is expected to vary with depth, we estimate M_c for different depth ranges using the GFT-95% method before choosing a fixed M_c = 0.3 to estimate the b values.

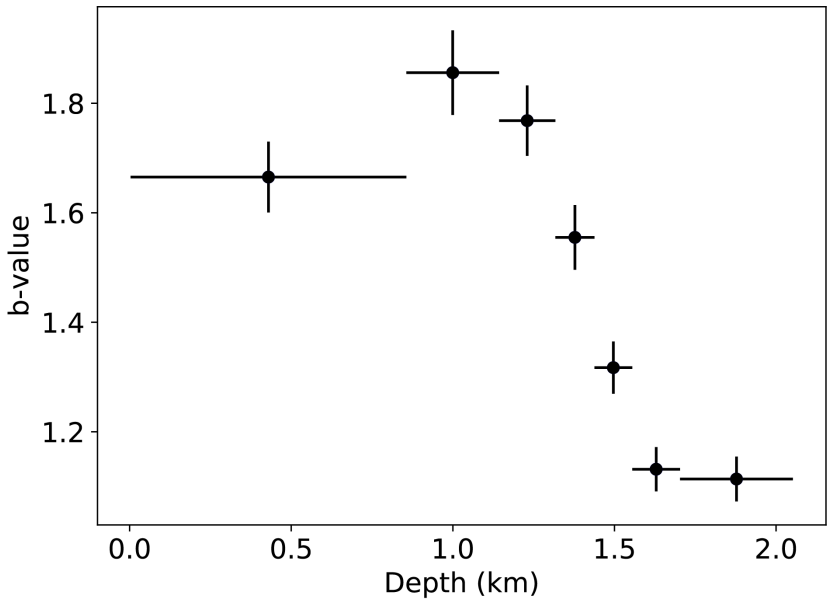

6. Figure S6

a, Cumulative number of events with depth for the lower tidal stress group (blue) and higher tidal stress group (red) (see Fig. 4). **b**, Mean (circle) and median (triangle) earthquake depth for non-overlapping stress bins of 4 kPa.

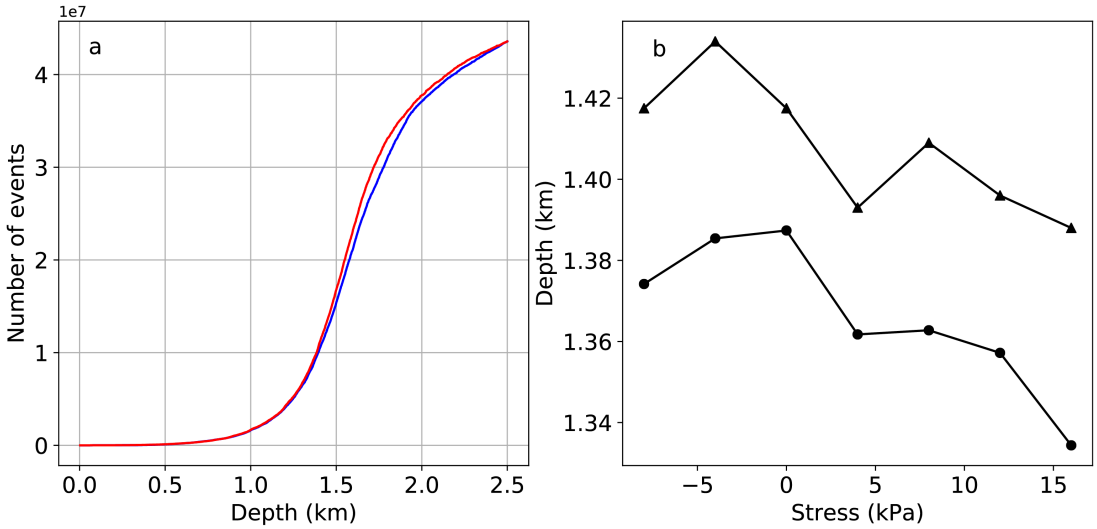

7. Figure S7

The normalized earthquake spatial distribution in 1 km^2 grids for **a**, lower tidal stress group and **b**, higher tidal stress group (see Fig. 4). **c**, The earthquake spatial distribution in 1 km^2 grids for all events above M_c = 0.3. Only grids containing more than 1,000 events are shown.

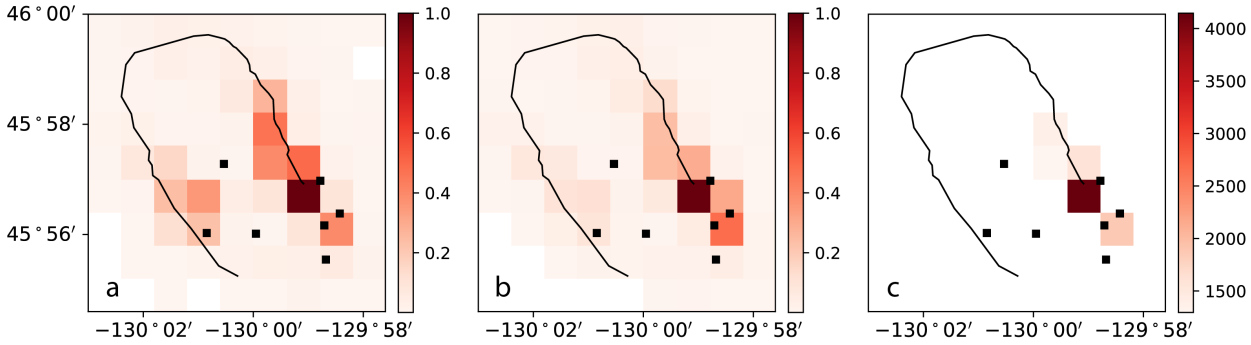

References

Shi, Y., Bolt, B.A., 1982. The standard error of the magnitude-frequency *b* value. Bull. Seismol. Soc. Am. 72 (5), 1677–1687.

Scholz, C.H., Tan, Y.J., Albino, F., 2018. The mechanism of tidal triggering of earthquakes at mid-ocean ridges. arXiv:1812.00639v1.